

Ionizing Electrons on the Martian Nightside: Structure and Variability

Robert J. Lillis, David L. Mitchell, Morgane Steckiewicz, David Brain, Shaosui Xu, Tristan Weber, Jasper Halekas, Jack Connerney, Jared Espley, Mehdi Benna, et al.

▶ **To cite this version:**

Robert J. Lillis, David L. Mitchell, Morgane Steckiewicz, David Brain, Shaosui Xu, et al.. Ionizing Electrons on the Martian Nightside: Structure and Variability. Journal of Geophysical Research Space Physics, 2018, 123, pp.4349-4363. 10.1029/2017JA025151 . insu-03678215

HAL Id: insu-03678215
https://insu.hal.science/insu-03678215

Submitted on 25 May 2022

HAL is a multi-disciplinary open access archive for the deposit and dissemination of scientific research documents, whether they are published or not. The documents may come from teaching and research institutions in France or abroad, or from public or private research centers.

L'archive ouverte pluridisciplinaire **HAL**, est destinée au dépôt et à la diffusion de documents scientifiques de niveau recherche, publiés ou non, émanant des établissements d'enseignement et de recherche français ou étrangers, des laboratoires publics ou privés.

Copyright

Check for updates

AGU100 ADVANCING EARTH AND SPACE SCIENCE

JGR

Journal of Geophysical Research: Space Physics

RESEARCH ARTICLE
10.1029/2017JA025151

Special Section:
Mars Aeronomy

Ionizing Electrons on the Martian Nightside: Structure and Variability

Robert J. Lillis[1], David L. Mitchell[1], Morgane Steckiewicz[2], David Brain[3], Shaosui Xu[1], Tristan Weber[3], Jasper Halekas[4], Jack Connerney[5], Jared Espley[5], Mehdi Benna[5], Meredith Elrod[5], Edward Thiemann[3], and Frank Eparvier[3]

[1]Space Sciences Laboratory, University of California Berkeley, Berkeley, CA, USA, [2]IRAP, Université de Toulouse, CNRS, UPS, CNES, Toulouse, France, [3]Laboratory for Atmospheric and Space Physics, University of Colorado Boulder, Boulder, CO, USA, [4]Department of Physics and Astronomy, University of Iowa, Iowa City, IA, USA, [5]NASA Goddard Space Flight Center, Greenbelt, MD, USA

Abstract The precipitation of suprathermal electrons is the dominant external source of energy deposition and ionization in the Martian nightside upper atmosphere and ionosphere. We investigate the spatial patterns and variability of ionizing electrons from 115 to 600 km altitude on the Martian nightside, using CO_2 electron impact ionization frequency (EIIF) as our metric, examining more than 3 years of data collected in situ by the Mars Atmosphere and Volatile EvolutioN spacecraft. We characterize the behavior of EIIF with respect to altitude, solar zenith angle, solar wind pressure, and the geometry and strength of crustal magnetic fields. EIIF has a complex and correlated dependence on these factors, but we find that it generally increases with altitude and solar wind pressure, decreases with crustal magnetic field strength and does not depend detectably on solar zenith angle past 115°. The dependence is governed by (a) energy degradation and backscatter by collisions with atmospheric neutrals below ~220 km and (b) magnetic field topology that permits or retards electron access to certain regions. This field topology is dynamic and varies with solar wind conditions, allowing greater electron access at higher altitudes where crustal fields are weaker and also for higher solar wind pressures, which result in stronger draped magnetic fields that push closed crustal magnetic field loops to lower altitudes. This multidimensional electron flux behavior can in the future be parameterized in an empirical model for use as input to global simulations of the nightside upper atmosphere, which currently do not account for this important source of energy.

Key Points:
- We investigate the patterns and variability of electron impact ionization frequency (EIIF) below 600 km on the Martian nightside
- EIIF generally increases with altitude and solar wind pressure and decreases with crustal magnetic field strength
- Patterns of EIIF reflect the combined solar wind-dependent topology of Mars' variable draped IMF and planet-fixed crustal magnetic fields

Correspondence to:
R. J. Lillis,
rlillis@ssl.berkeley.edu

Citation:
Lillis, R. J., Mitchell, D. L., Steckiewicz, M., Brain, D., Xu, S., Weber, T., et al. (2018). Ionizing electrons on the Martian nightside: Structure and variability. *Journal of Geophysical Research: Space Physics*, *123*, 4349–4363. https://doi.org/10.1029/2017JA025151

Received 22 DEC 2017
Accepted 2 MAY 2018
Accepted article online 15 MAY 2018
Published online 28 MAY 2018

©2018. American Geophysical Union. All Rights Reserved.

1. Introduction

Electron precipitation is the dominant external energy source in the nightside upper atmosphere of Mars. Suprathermal electrons, originating in the solar wind and bound to magnetic field lines, precipitate into the atmosphere from either the turbulent magnetosheath or the induced magnetotail and collide with neutral atoms and molecules. Elastic collisions are most common but cause negligible heating due to the large difference in masses (Lillis et al., 2009). Inelastic collisions result in the target neutral undergoing one or more of the following: excitation into higher electronic states, ionization and the consequent release of an electron, and dissociation of molecules into constituent atoms and molecules.

These processes have several consequences: (1) auroral emission occurs via the decay of excited states (Bertaux et al., 2005; Schneider et al., 2015), (2) a patchy and variable nightside ionosphere is formed (Girazian, Mahaffy, Lillis, Benna, Elrod, Fowler, et al., 2017; Girazian, Mahaffy, Lillis, Benna, Elrod, & Jakosky, 2017; Lillis et al., 2011, 2009; Němec et al., 2011, 2010; Safaeinili et al., 2007), (3) the resulting plasma interacts with Mars' inhomogeneous crustal magnetic fields and neutral winds to produce rich and complex electrodynamics (Fillingim et al., 2010, 2012; Riousset et al., 2014), (4) newly formed planetary ions can be accelerated (a) to escape velocity (Brain et al., 2015; Dong et al., 2015; Dubinin et al., 2017; Lundin et al., 2011, 2013, 2008, 1989) or (b) back into the atmosphere, causing sputtering escape (Leblanc et al., 2015; Luhmann et al., 1992), and (5) ions can also recombine with electrons dissociatively, resulting in escape of hot neutral oxygen (Fox & Hać, 2009; Lee et al., 2015; Lillis et al., 2017), nitrogen and carbon (Fox & Bakalian, 2001; Lee et al., 2014). These last two processes contribute to atmospheric and climate evolution (Lillis et al., 2015). With this array of consequences, it is important for us to understand the structure and dynamics of suprathermal electrons on the nightside of Mars, and how they vary spatially, with respect to

the crustal magnetic fields which rotate with the planet, and temporally with respect to external heliospheric drivers.

Electron dynamics on the Martian nightside have been studied via several approaches over the last 15 years. Electron energy spectra and pitch angle distributions (PADs) were measured by the Mars Global Surveyor Magnetometer/Electron Reflectometer (MAG/ER) from a near-circular orbit at 370–430 km altitude and 2 a.m./2 p.m. local time from 1999 to 2006 (Mitchell et al., 2001). PADs allowed the topology (i.e., whether the ends of the magnetic field line connect to the collisional atmosphere) of the local magnetic field line to be determined and mapped (Brain et al., 2007; Lillis et al., 2004, 2008). Lillis et al. (2011) constructed maps of downward electron flux measured by MAG/ER with models of the crustal magnetic field and neutral atmosphere to simulate three-dimensional ionization rates below 400 km on the Martian nightside in the region of strongest crustal magnetic field (20°–80°S, 140°–220°E). Lillis and Brain (2013) mapped the measured nightside downward electron flux globally and how precipitation patterns varied with proxies for the solar wind pressure and interplanetary magnetic field. Lillis and Fang (2015) modeled how the interplay between the electron energy and pitch angle at ~400 km and the strength of the crustal magnetic field affects nightside vertical profiles of ionization rates. Shane et al. (2016) compared MAG/ER-measured upward and downward electron fluxes to study energy deposition on the Martian nightside.

However, while enlightening, these studies were always fundamentally limited by Mars Global Surveyor's orbit, fixed in altitude and local time. In contrast, the Mars Atmosphere and Volatile EvolutioN (MAVEN) mission was given an orbit specifically designed to sample all relevant plasma and upper atmosphere regions in near-Mars Space (Jakosky et al., 2015). On board MAVEN is the Solar Wind Electron Analyzer (Mitchell et al., 2016) or SWEA, data from which have enabled further studies of the dynamics of suprathermal electrons. Steckiewicz et al. (2015) and Steckiewicz et al. (2017) examined suprathermal electron depletions on the nightside and concluded that absorption by CO_2 was their main cause below 170 km and exclusion by strong crustal fields was their main cause above 170 km. Xu et al. (2016) discovered photoelectrons transported from the dayside to below 200 km on the nightside (where they caused ionization) via long magnetic loops. Xu et al. (2017) used SWEA energy spectra to map magnetic topology of open field lines at different altitudes on the dayside and nightside, while Weber et al. (2017) used SWEA PADs to study the frequency and geographic distribution of open and closed field lines (i.e., connected to the collisional atmosphere at one and both ends, respectively).

In this paper, we characterize electron impact ionization frequency (EIIF) on the nightside of Mars, and its variability (a) with respect to planetary variables such as altitude, solar zenith angle, local time and geography, (b) with respect to in situ measured strength and elevation angle of the magnetic field lines to which the electrons are bound, and (c) with respect to solar wind pressure, which is converted to magnetic pressure inside the bow shock (Nagy et al., 2004). Section 2 describes the data sets we will use, the calculation of EIIF, and the physical processes that should affect it. Section 3 shows and describes our results, consisting of line plots and color plots showing ionizing energy flux as a function of the aforementioned variables. Section 4 contains discussion of these results and our conclusions respectively.

2. Data

We utilize more than 3 years of in situ data, collected from 1 November 2014 to 1 February 2018, by the MAVEN spacecraft (Jakosky et al., 2015), collected at altitudes between 115 and 600 km at a range of solar zenith angles and local times as MAVEN's elliptical orbit (~6,200 km apoapsis altitude, ~150 km periapsis altitude, with occasional "deep dips" down to ~120 km altitude) precessed around the planet. Below we describe our primary metric and data sources.

2.1. Primary Metric: CO_2 Electron Impact Ionization Frequency (EIIF)

The Solar Wind Electron Analyzer (SWEA) is a hemispherical electrostatic analyzer of top-hat design on a fixed boom, measuring electron flux at 4 s cadence, over energies from 3 eV to 5 keV, 360° in azimuth and ±60° in polar angle (totaling 87% of the sky), as described in detail by Mitchell et al. (2016). For this study, we are interested in suprathermal electrons' capacity to ionize neutrals. Thus, one possible metric to study would be the total integrated number flux of electrons above a relevant ionization threshold (e.g., 13.6 eV for CO_2), that is, ionizing electron flux (#/cm^2/s/sr). Another would be integrated ionizing electron energy flux (eV/cm^2/s/sr), which gives greater weight to higher-energy electrons, taking account of their ability to cause multiple

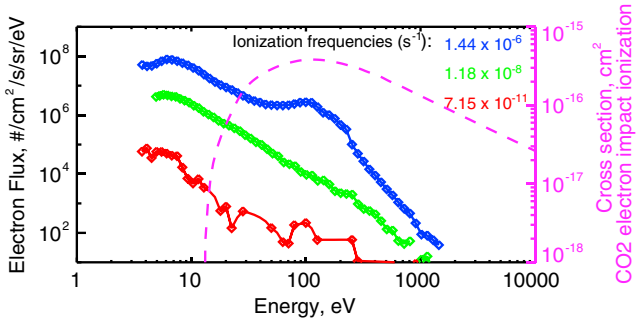


Figure 1. Example calculation of electron impact ionization frequency producing CO_2^+ ions. Blue, green, and red are three typical electron flux spectra seen on the Martian nightside. Electron impact ionization frequency is the integral over energy of the product of these spectra with the cross section (pink).

ionizations. However, both of these overestimate the higher-energy electrons' capacity to ionize because they do not take account of the energy dependence of ionization cross sections, and the latter even more so because it counts subsequent ionizations from higher-energy electrons, which are not occurring locally.

Instead, we directly calculate EIIF, in units of number per second, by multiplying energy spectra of omnidirectional differential electron number flux (#/cm^2/s/sr/eV), measured every 4 s by SWEA (see Mitchell et al., 2016, for how this is calculated from raw data), by the cross section for ionization by electron impact (cm^2) from the cross-section database of Sung and Fox (2000), and integrating over energy and multiplying by 4π. Figure 1 shows three examples of calculating EIIF for CO_2 from three representative electron energy spectra measured by SWEA on the Martian nightside. Blue is a typical accelerated electron spectrum (in this case with a "bump" or beamed component around 120 eV) of the type observed by Mars Global Surveyor (Brain et al., 2006) and known to cause discrete aurora as observed by Mars Express (Bertaux et al., 2005; Leblanc et al., 2006). Green is a weaker but still commonly observed magnetotail spectrum (e.g., Lillis et al., 2011). Red is not far above the noise level of the instrument and commonly seen in plasma "voids" on the nightside, that is, regions of closed crustal magnetic field lines whose topology excludes most suprathermal electrons (Brain et al., 2007).

Because it will be cumbersome to show ionization frequencies for all four primary thermospheric neutral species (CO_2, O, N_2, and CO), we choose CO_2 as it is the dominant neutral below ~200 km and because its electron impact ionization cross section is not qualitatively different from that of the other species (see Figure 2), particularly atomic oxygen that dominates above ~200 km.

Note that these ionization frequencies can be easily converted to volume ionization rates by simply multiplying by the density (e.g., #/cm^3) of the target neutral species, which the Neutral Gas and Ion Mass Spectrometer (NGIMS) instrument (Mahaffy et al., 2014) also measures in situ, that is, CO_2 in the example. However, we do not show ionization rates in this paper for two reasons: (1) we wish to analyze the patterns and variability of the ionizing suprathermal electrons independent of the exponentially decreasing (with altitude) neutral density and its variability and (2) reliable neutral density measurements from NGIMS often do not exceed 300 km in altitude.

2.2. Physical Process Effects on EIIF

Before we continue, we present a brief note about explaining the behavior of EIIF data in terms of the dynamics of suprathermal electrons. As shown in Figure 1, EIIF is sensitive only to fluxes of electrons above the ionization threshold of Mars' atmospheric neutrals. Therefore, without any prior knowledge of likely causes, an increase or decrease in EIIF could be explained as either an overall decrease in suprathermal electron flux due to an energy-independent process like magnetic mirroring or an energy-dependent process such as inelastic scattering, electrostatic acceleration/deceleration or wave-particle acceleration. Our interpretation of the behavior of EIIF will focus on the effects of the physical processes we know are occurring, can easily identify, and with respect to which we can categorize EIIF straightforwardly: (a) interactions with magnetic fields (crustal and induced), which can be measured and which cannot change electrons' energies because magnetic fields cannot do work, and (b) scattering by atmospheric neutrals, which varies exponentially with altitude and which both (i) reduces overall fluxes of precipitating electrons through elastically scattering them back up into space and (ii) degrades electrons' energy through inelastic scattering processes such as ionization, excitation and dissociation. In contrast, it is beyond the scope of this work to identify (and sort EIIF by) signatures of electrostatic

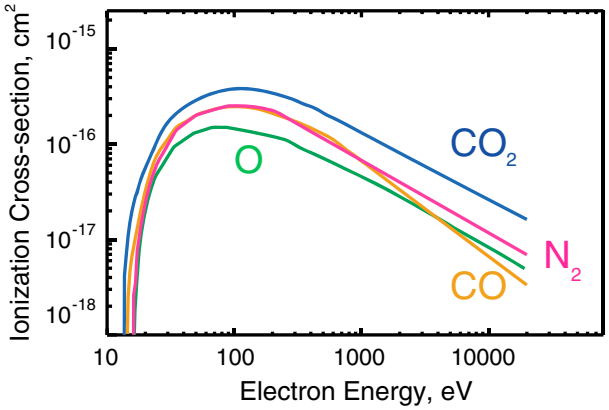


Figure 2. Electron impact ionization cross sections are plotted as a function of energy for the four major Martian thermospheric neutral species (Sung & Fox, 2000).

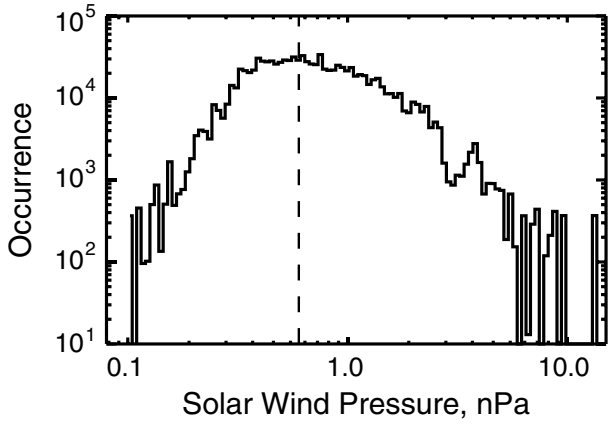


Figure 3. Histogram of all the solar wind pressure measurements made during this time, with the median (vertical dashed line) shown at 0.65 nPa.

acceleration (e.g., via a detailed analysis of the energy dependence of electron loss cones; potentials can on rare occasions be up to ~20 V, Lillis et al., 2018, but are typically <2 V, Collinson et al., 2015) or wave-particle acceleration (via wave and resonance analysis, e.g., Fu et al., 2011).

2.3. Other Data Sources

We utilize data from four additional MAVEN instruments, as well as spacecraft ephemeris data, in order to characterize the behavior of EIIF. First, we use magnetic field vectors measured by the magnetometer (MAG), which consists of two triaxial fluxgate magnetometers (inboard and outboard) located at the ends of small "diving boards" affixed to the end of each solar panel, as described by Connerney et al. (2015). As a metric for the strength of the magnetic field due specifically to crustal magnetism at a given geographic location, we use the magnetic field magnitude evaluated at 400-km altitude by the spherical harmonic crustal field model of Morschhauser et al. (2014).

Second, we use measurements of the upstream solar wind pressure measured by the Solar Wind Ion Analyzer (SWIA) outside the Martian bow shock. SWIA is also a top-hat electrostatic analyzer, measuring ions between 25 eV and 30 keV, over all azimuth angles and an energy-dependent range of polar angles <45°. The instrument is described in detail by Halekas et al. (2015) and the automated method of determining whether a given measurement is outside the bow shock is described by Halekas et al. (2017). Figure 3 shows a histogram of all solar wind pressure measurements used in this study.

Third, we calculate mass densities from number densities of neutral CO_2, O, N_2 CO, and Ar measured by the NGIMS (Mahaffy et al., 2014). Fourth, as a metric for the ability of solar extreme ultraviolet (EUV) to create photoelectrons on the Martian dayside (which can travel to the nightside), we use daily values of CO_2 photoionization frequency calculated using the method described by Lillis, Deighan, Fox, Bougher, et al. (2017) from the Flare Irradiance Spectral Model for Mars (FISM-M) model of solar spectral irradiance (Thiemann et al., 2017) which is fed by measurements from MAVEN's Extreme Ultraviolet Monitor (EUVM) (Eparvier et al., 2015). Lastly, all altitudes quoted in this paper are geodetic (areodetic), that is, measured perpendicular to the surface of an oblate spheroid that best fits the Martian geoid (areoid). In addition, EIIF will be used as shorthand for electron impact ionization frequency and all references to impact ionization frequencies will be for CO_2.

3. Results: Nightside Electron Impact Ionization Frequency

In this section we first examine the spatial pattern of CO_2 EIIF Martian nightside with respect to solar zenith angle (SZA) and altitude, and how that pattern depends on solar wind pressure, regional crustal magnetic field strength and local time (i.e., dawn versus dusk). We then collapse the SZA dimension and look at how the altitude dependence of EIIF on the deep nightside (SZA > 120°) varies more finely with solar wind pressure and regional crustal field strength, as well as geographically with respect to strong and weak crustal field regions of the planet. Next, we look at how EIIF depends on solar wind pressure and solar EUV, independent of effects of atmospheric scattering of electrons or crustal magnetic field. Lastly, we examine its behavior with respect to local magnetic field strength and geometry, in different altitude ranges.

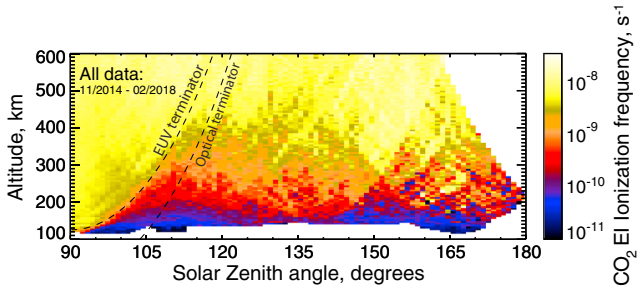


Figure 4. CO_2 electron impact ionization frequency on the Martian nightside, measured between 1 November 2014 and 1 February 2018, binned as a function of solar zenith angle (1° bins) and altitude (5-km bins). The black dotted and dashed lines are the optical and extreme ultraviolet terminators (assuming a spherical planet with Mars' mean radius of 3,389.9 and 3,389.9 + 122.5 km, respectively, Steckiewicz et al., 2017).

3.1. Solar Zenith Angle, Altitude, and Local Time Dependence of EIIF

First, we wish to visualize and examine how EIIF varies as we move across the terminator and into the nightside. Figure 4 shows all the data together, illustrating that the average EIIF is fairly uniform where solar EUV produces photoelectrons, that is, to the left of the black dashed line (with the exception of altitudes below ~140 km where the density of neutral CO_2 is sufficient to absorb a substantial fraction of solar EUV, thus decreasing the production of photoelectrons,

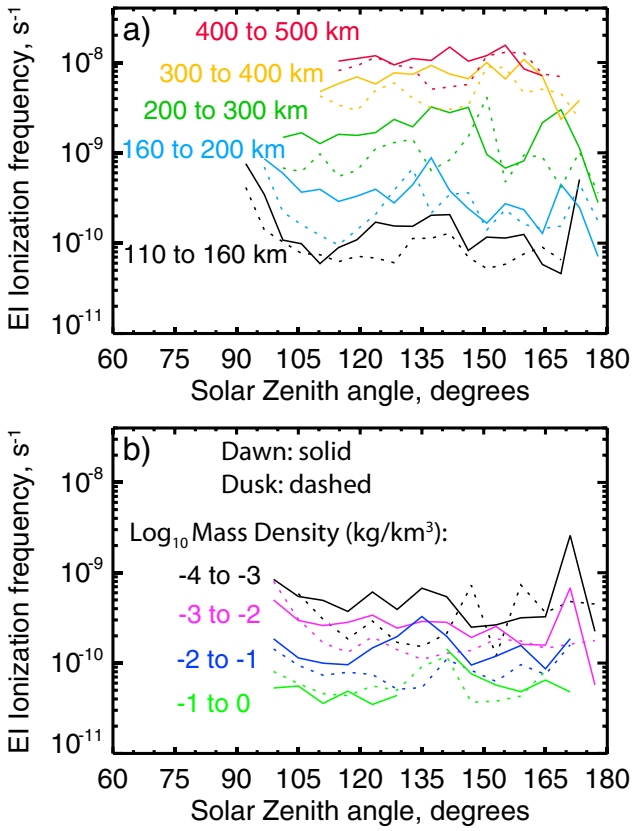


Figure 5. CO_2 electron impact ionization frequency as a function of solar zenith angle is plotted separately for dawn (solid lines) and dusk (dashed lines), for five different altitude ranges (colors, top panel) and four different mass density ranges (colors, bottom panel).

Steckiewicz et al., 2015). The origin of these ionizing electrons depends on altitude. In the collisional atmosphere below ~200 km, they are mostly photoelectrons produced nearby, whereas at higher altitudes they are a combination of magnetosheath electrons and photoelectrons transported from the collisional atmosphere upward along magnetic field lines (e.g., Xu et al., 2017).

As we move across the EUV terminator, we see a marked decrease in overall EIIF, at least below ~400 km. This is expected at low altitudes (below ~200 km) since there is no longer significant solar EUV irradiance to produce local photoelectrons. However at higher altitudes, this flux decrease across the terminator is most easily explained by magnetic field geometry and topology since electrons cannot easily move across magnetic field lines and thus electrons' access to these regions is retarded. Two related factors combine to comprise this magnetic configuration across the terminator and thus affect the access that electrons, flowing either across the terminator from the dayside or planetward along the magnetotail, have to lower altitudes: (1) the global pattern of the draping of the interplanetary magnetic field around Mars and (2) crustal magnetic fields, which rotate with the planet and which exclude sheath or tail electrons where their topology is closed (i.e., connected to the atmosphere at both ends, Brain et al., 2007). We explore these factors in section 3.2.

We also wish to examine how the pattern shown in Figure 4 varies between dawn and dusk sides, given that the manner in which the interplanetary magnetic field (IMF) piles up and drapes around the planet is to some degree dependent on the IMF cone angle (i.e., the angle between the Mars-sun line and the IMF direction), which has a preferred value near 57° (e.g., Riedler et al., 1989). Because SZA-altitude color plots appear quite similar for dawn versus dusk, instead, we use line plots to compare, as shown in Figure 5. In panel (a) we notice that the asymmetry between dawn and dusk is altitude-dependent and appears to have two components: (1) a "bulge" exists at all altitudes where dawn fluxes are higher than dusk by a factor of 2–4 in the range $125° < SZA < 145°$, with the bulge at slightly lower SZA for lower altitudes, largest at 200–300 km and smallest at lower and higher altitudes, (2) closer to the terminator ($SZA < 125°$), a consistent dawn-dusk asymmetry exists below 200 km with dawn fluxes higher than dusk by a factor of ~1.5–2.

The asymmetry bulge at $125° < SZA < 145°$ has no obvious explanation and has not been observed in models. In contrast, the near-terminator asymmetry below 200 km is explained by the a well-known asymmetry in neutral density whereby the atmosphere is warmer at dusk compared with dawn and therefore sits higher (Elrod et al., 2017) and thus absorbs more electron flux at the same altitude, resulting in lower EIIF at dusk versus dawn. We confirm this to be the case by making the same type of plot, but with respect to neutral mass density, as shown in Figure 5b, where we note that no significant asymmetry is apparent for $SZA < 125°$ but the bulge is still visible at all mass densities up to 0.1 kg/km^3. (Note that mass density measurements on the nightside rarely exceed 300 km altitude due to the sensitivity of the NGIMS instrument).

3.2. Variability of SZA and Altitude Dependence of EIIF Jointly With Solar Wind Pressure and Crustal Magnetic Field

To separate the effects on EIIF of the IMF draping around Mars and the crustal magnetic fields, we separate the SZA and altitude dependence of EIIF by (a) the strength of the crustal magnetic field at 400 km altitude as determined by the crustal field model of Morschhauser et al. (2014) ("weak": 0–3 nT, "moderate": 3–15 nT and "strong": >15 nT, comprising 29.5%, 47.0%, and 23.5% of Mars' surface area, respectively) and (b) the solar wind pressure (<0.6 and > 0.6 nPa), as shown in Figure 6. For the latter, note that solar wind dynamic pressure outside the bow shock is converted to magnetic pressure in this draped field region we examine, resulting in stronger mean draped magnetic fields for higher solar wind pressures than for lower pressures. To

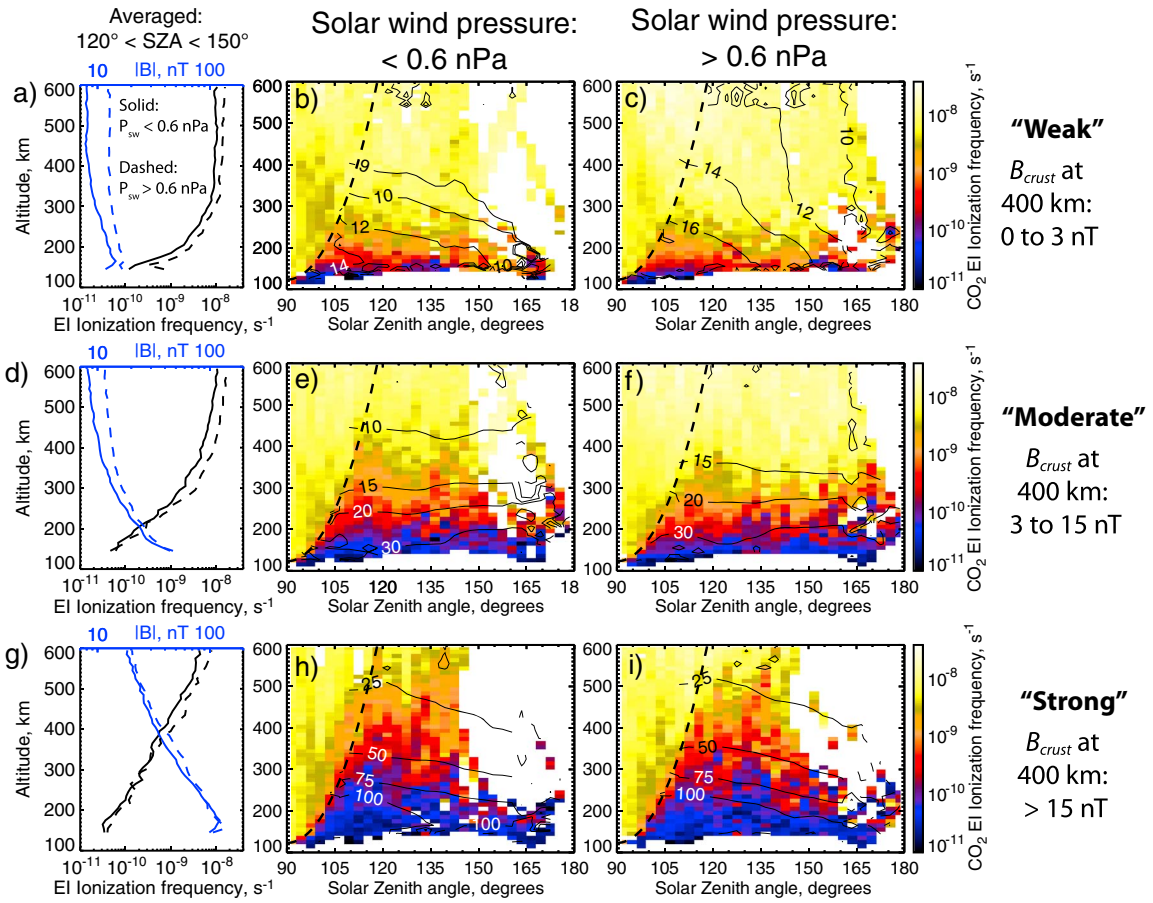


Figure 6. CO_2 electron impact ionization frequency is binned as a function of solar zenith angle (SZA) and altitude. The six color panels show the same data as Figure 4 but in coarser bins (3° in SZA and 10 km in altitude) and divided up by the strength of the crustal magnetic field at 400 km above or below each measurement at the same geographic location (rows: 0–3, 3–15, and >15 nT per the model of Morschhauser et al., 2014) and solar wind pressure (columns: <0.6 and >0.6 nPa). Thin labeled contours are average magnetic field values measured in situ. The associated line plots in the left-hand column show EIIF (black) and in situ magnetic field strength (blue) averaged over 120° < SZA < 150°, for solar wind pressures below (solid) and above (dashed) 0.6 nPa.

maintain adequate statistics, these are more coarsely binned than Figure 4 but still quite clearly show that EIIF across the terminator and in the nightside show a significant dependence on these two factors. Contours of locally measured total magnetic field are added for context.

The first thing we notice is that average nightside EIIF depends strongly on crustal magnetic field strength and that the influence of the crustal fields decreases with altitude. At 600 km, there is little difference (<20%) between the weak and moderate crustal field cases (compare Figures 6a and 6d), because in both cases the crustal fields at this altitude are too weak in comparison to the piled up, draped magnetic field (~8–13 nT) to influence magnetic geometry and hence the accessibility of suprathermal electrons. We can call this the "unhindered" EIIF level (~10^{-8} s^{-1}). In contrast, fluxes are a factor of ~2 lower at 600 km for the strong field case where the crustal fields at 600 km are comparable to or larger than the draped field. As altitudes decrease, the crustal fields increase in importance with respect to the draped field and thus progressively exclude the suprathermal electrons that cause ionization, thus decreasing EIIF. At 350 km, in the weak crustal field case, EIIF is still at the unhindered level, but a factor of ~3 lower than this in the moderate case and a factor of ~30 lower in the strong case. Below 300 km, even the weak crustal fields cause a decrease in flux with altitude (Figure 6b), although absorption and scattering by atmospheric neutrals also plays a role below ~220 km (Lillis & Fang, 2015).

We also note a dependence on solar wind pressure, which takes two forms. First, we see a moderately but consistently higher (~30%) unhindered EIIF for higher solar wind pressures compared to lower pressures, as can be seen in Figure 6a, which is expected due to higher and/or more energetic fluxes of sheath and

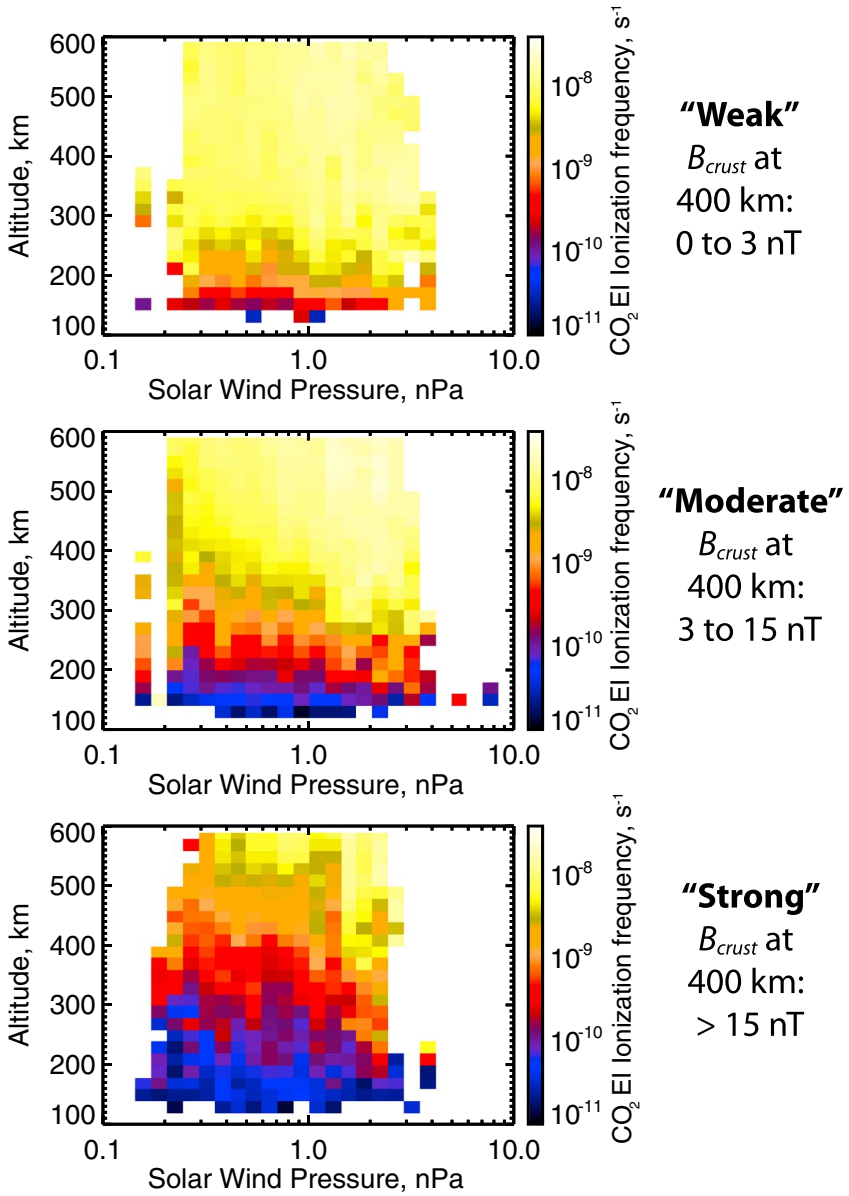


Figure 7. CO_2 electron impact ionization frequency is plotted as a function of altitude and solar wind pressure, for SZA > 115°, for the same three ranges of regional crustal magnetic field strength, and with the same color scale, as shown in Figure 6. SZA = solar zenith angle.

tail electrons which themselves originate in the solar wind (we will examine this further in section 3.4). Second, we see the effect of solar wind pressure converted to magnetic pressure, resulting in higher draped mean magnetic fields for higher solar wind pressures than for lower pressures (~8 and ~13 nT for P_{sw} < 0.6 and > 0.6 nPa, respectively). Stronger draped fields (from higher pressures) magnetically connect with crustal fields down to lower altitudes, that is, pushing closed magnetic field loops (which exclude suprathermal electrons) to lower altitudes and thus increasing the flux of electrons that cause ionization (as demonstrated previously at ~400 km and 2 a.m. local time by Lillis & Brain, 2013) and hence EIIF. As was mentioned in section 2.2, when only considering the effects of magnetic topology as we do here, EIIF should not change due to shifts in the omnidirectional electron energy spectrum because magnetic fields do no work.

Interestingly, the effect just described is least pronounced where the crustal fields are both weakest and strongest in comparison to the draped field, as can be seen in the six color plots of Figure 6, but most clearly in the left column of line plots. For weak crustal field regions, the EIIF for low and high solar wind pressures do

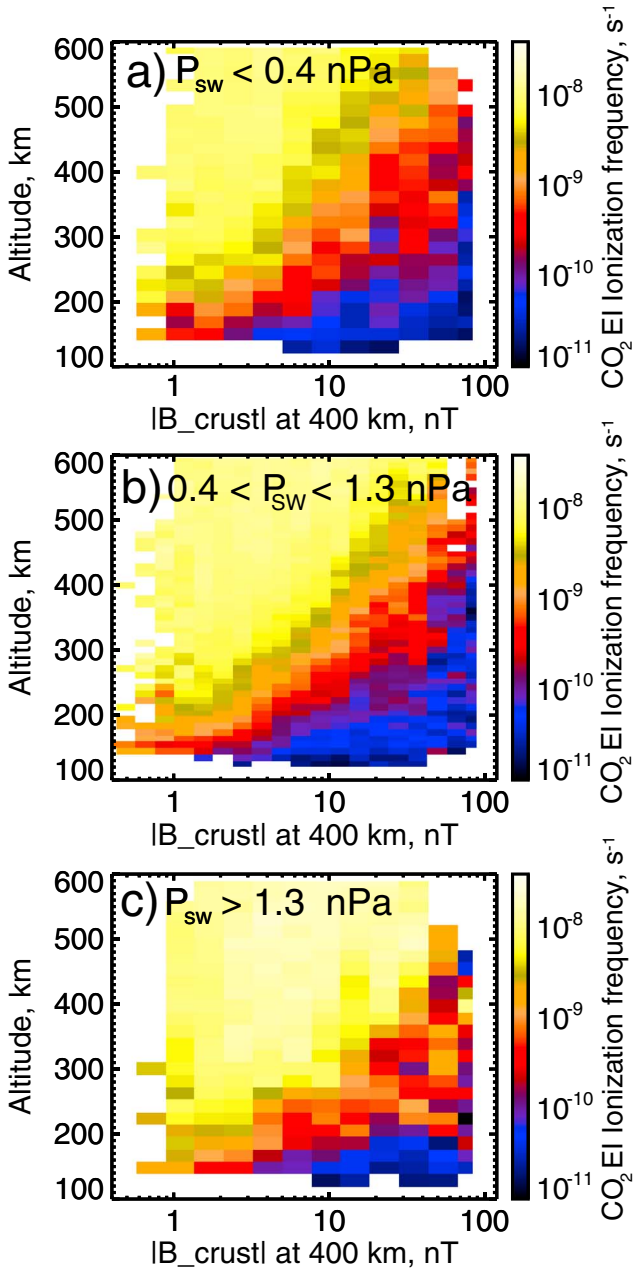


Figure 8. CO_2 electron impact ionization frequency is binned as a function of altitude and crustal magnetic field strength at 400 km (i.e., above or below each measurement at the same latitude/longitude) per the model of Morschhauser et al. (2014) for SZA > 115° for three separate ranges of solar wind pressure (<0.4, 0.4–1.3, and >1.3 nPa), and with the same color scale as shown in Figure 6. The resolution in each panel is determined by the number of available data points. SZA = solar zenith angle.

not diverge significantly until altitudes below ~160 km (see black solid and dashed lines in Figure 6a), where even weak crustal fields are in many cases comparable to or can exceed the 8–13 nT draped field. For moderate crustal field regions (Figures 6d–6f), the EIIFs for low and high solar wind pressures diverge clearly between ~250 and 400 km. This is expected as the draped IMF at these altitudes are comparable to the crustal fields (averaging ~15 nT at 250 km to ~8 nT at 400 km), that is, the stronger draped IMF resulting from higher solar wind pressures pushes the closed crustal loops downward sufficiently to allow more ionizing electrons to reach lower altitudes (resulting in higher EIIF) than does the weaker draped IMF resulting from lower solar wind pressures.

For strong crustal field regions (Figures 6g–6i), above ~350 km this ~4–5 nT average difference between low and high pressures is a sufficient fraction of the crustal field strength to allow higher EIIF for higher solar wind pressures. However below ~350 km, the crustal fields are strong enough that the access of ionizing electrons (and hence the EIIF level) is unaffected by the strength of the draped field, that is, unaffected by the solar wind pressure.

Figure 6 is plotted in the easily visualized parameter space of SZA and altitude but that comes at the expense of resolution in solar wind pressure and crustal magnetic field strength. Therefore, in order to examine the altitude dependence of average EIIF with respect to these two variables intuitively and at finer resolution, Figures 7 and 8 collapse the SZA variable down and plot the altitude dependence of EIIF with respect to solar wind pressure and the crustal magnetic field magnitude at 400 km (i.e., above or below each measurement as per the model of Morschhauser et al., 2014), respectively. These figures are consistent with Figure 6 with additional detail revealed. Figure 7a confirms that, where crustal fields are weak (<3 nT at 400 km, totaling 29.5% of the surface), EIIF is weakly dependent on solar wind pressure except at the very lowest altitudes, while Figure 7b shows that for regions of moderate crustal magnetic field strength (3–15 nT at 400 km, totaling 47% of Mars' surface area), the altitude dependence of EIIF varies over the entire range of solar wind pressures, from lowest to highest, highlighting the dynamic and variable nature of the nightside suprathermal electron environment.

We use the solar wind dependence apparent in Figure 7b to choose the ranges of solar wind pressure for which to plot EIIF as a function of altitude and crustal field strength in Figure 8: 0–0.4, 0.4–1.3, and >1.3 nPa. These plots show that the altitude dependence of average EIIF varies over most of the range of crustal magnetic field strengths that exist at 400 km. For the very weakest crustal field strengths of <~1.5 nT at 400 km, crustal fields essentially do not impact EIIF, whose altitude dependence is affected primarily by absorption of suprathermal electrons by the neutral atmosphere below ~220 km. However, for all crustal field strengths above ~1.5 nT, the crustal fields reduce EIIF at higher and higher altitudes as the crustal field strength increases, with this dependence being less pronounced for higher solar wind pressures. These higher pressures, as discussed earlier, push the closed crustal fields downward and therefore lessen their ability to exclude ionizing electrons.

3.3. Geographic Dependence of Nightside EIIF

The previous section demonstrated that deep nightside (SZA > 115°) EIIF has a complex dependence but generally increases with altitude and solar wind pressure, decreases with crustal magnetic field strength, and does not depend detectably on solar zenith angle. Another, and perhaps more intuitive, way to

visualize the effect of the planet-fixed crustal magnetic fields is to make geographic maps of EIIF. Lillis and Brain (2013) made high resolution (1° × 1°) maps of electron fluxes above 100 eV at 2 a.m. local time from more than 32,000 near-circular sun synchronous orbits of the MGS spacecraft at ~400 km altitude over 7.5 years. These maps revealed in fine geographic detail the exclusion of suprathermal electrons from closed magnetic field regions and how the area of those closed field regions at ~400 km shrank as solar wind pressure increased, compressing the closed crustal fields toward the surface. With MAVEN's ~6,000 precessing elliptical orbits, we do not have nearly as much data at any one altitude or local time but have the advantage of a range of altitudes at which to make maps of nightside EIIF. Figure 9 shows these 15° × 15° maps, revealing the average geographic patterns of these fluxes and how they vary with respect to altitude (<160, 160–200, 200–300, 300–400, and 400–500), solar wind pressure (<0.6 and >0.6 nPa, the same as in Figure 6) and contours of crustal magnetic field magnitude at 400 km (10, 20, 50, 100 nT) shown in green.

These maps display many of the same features shown in Figures 6–8, but geographically. In particular we notice the generally lower EIIF in regions of crustal magnetic field but to a degree that as discussed earlier, depends on altitude, crustal field strength (normalized to 400 km altitude), and solar wind pressure. First, below 300 km, most regions with crustal magnetic fields >20 nT have noticeably lower EIIF (factors of 3–5) than regions where fields are <10 nT, with the lowest EIIF in the strongest field regions. Second, EIIF is higher for higher solar wind pressures, particularly in areas of moderate crustal field as the closed crustal field loops are pushed to lower altitudes by the stronger draped IMF that results from higher solar wind pressures. Third, the ability of the crustal fields to exclude suprathermal electrons and hence decrease EIIF diminishes for altitudes above 300 km, particularly for higher solar wind pressures: for example, in the upper right panel (400–500 km, >0.6 nPa), only a small area near the strongest crustal fields in the southern hemisphere still has low fluxes; the crustal fields have little influence elsewhere. Last, we see significantly lower EIIF below 200 km and particularly 160 km, likely due mostly to inelastic collisions with neutrals, which shift the electron spectrum to lower energies (therefore lowering EIIF) and elastic collisions with neutrals, which backscatter suprathermal electrons up out of the atmosphere, reducing the fluxes and hence EIIF.

3.4. Dependence on Solar Wind Pressure and Solar EUV Irradiance

So far we have seen that higher solar wind pressures reduce the ability of crustal fields to lower nightside EIIF. However, as mentioned in section 3.2 and seen in Figure 6a, higher solar wind pressures create higher EIIF even in situations where crustal field effects are negligible. This is not surprising given that some fraction of nightside ionizing electrons themselves originate in the solar wind. However, some are created in the dayside ionosphere as photoelectrons, primarily at 22 and 27 eV and are transported along draped magnetic field lines into the tail, as shown by Xu et al. (2016). Therefore, it is useful to briefly examine how unperturbed EIIF depends on both solar wind pressure and the solar EUV irradiance that produces photoelectrons on the dayside. It is beyond the scope of this paper to attempt to formally separate electrons by origin; in any case such a separation is not trivial due to acceleration/deceleration of electrons by field aligned potentials (Collinson et al., 2015; Lillis et al., 2018), which may blur and/or shift photoelectron peaks.

As a metric to best reflect the ability of solar EUV to produce photoelectrons in the dayside ionosphere, we use CO_2 photoionization frequency as described in section 2.3, instead of EUV irradiance at a single wavelength or integrated over a range of wavelengths. Figure 10 shows binned averages of EIIF as a function of CO_2 solar photoionization frequency and solar wind pressure for conditions unperturbed by atmospheric backscatter or crustal fields, that is, above 350 km in regions where B_{crust} at 400 km < 3 nT (see Figures 6a–6c and 7), a total of ~33,000 data points. Figure 10a divides up this data into low and high solar wind pressures, along with log-linear fits to these data. These fits show no statistically significant dependence of EIIF on CO_2 solar photoionization frequency. A slight positive dependence on solar wind pressure (i.e., the red dotted line is higher than the blue line) is generally consistent with the 15–20% larger flux for higher solar wind pressure seen in Figure 6a (black dashed versus solid lines).

These trends allow us to draw two conclusions. First, EIIF on the Martian nightside is dominated by solar wind electrons, not photoelectrons. Second, these effects are much smaller than the effects of crustal fields which are the main focus of this paper.

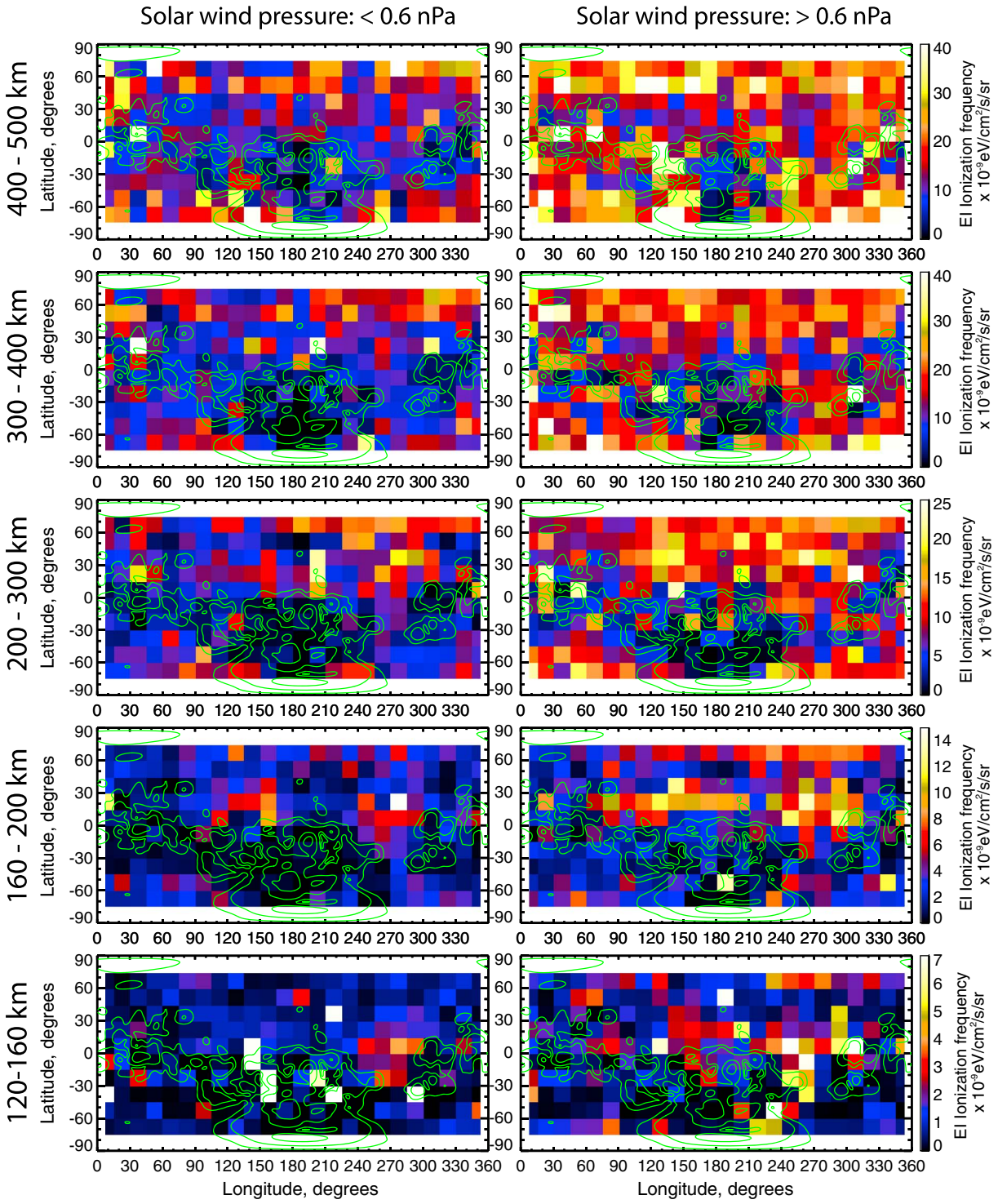


Figure 9. Mean electron impact ionization frequency is plotted in 15° bins of latitude and longitude for SZA >115°, separately by altitude range (rows: 120–160, 160–200, 200–300, 300–400, 400–500 km) and solar wind pressure (columns: <0.6 and >0.6 nPa). Overplotted in green is crustal magnetic field magnitude at 400 km per the model of Morschhauser et al. (2014), in contours of 10, 20, 50, and 100 nT. Note the color scale is *not* logarithmic and is different for each altitude range to bring out the geographic pattern of electron fluxes. SZA = solar zenith angle.

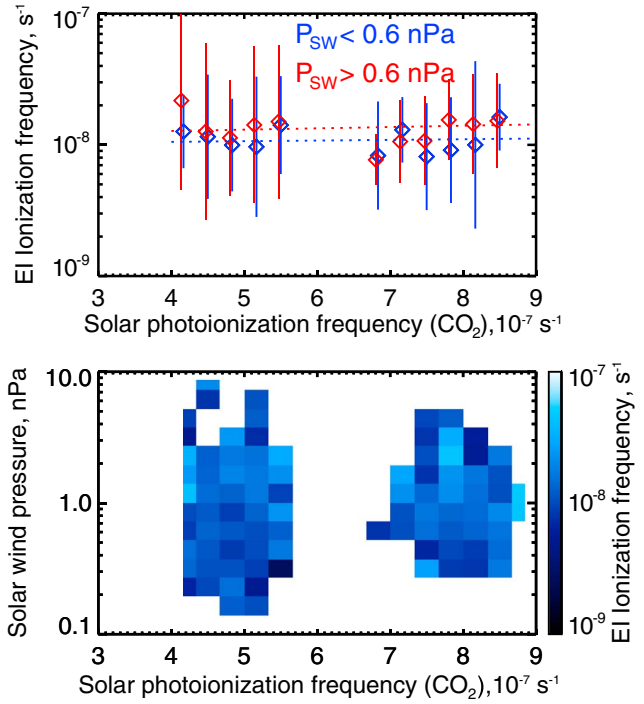


Figure 10. Dependence of "unperturbed" electron impact ionization frequency, that is, collected above 350-km altitude where crustal fields are weak (B_{crust} at 400 km < 3 nT, as in Figures 6a–6c and Figure 7a) on solar wind pressure and CO_2 solar photoionization frequency. Panel (a) shows binned averages for high (>0.6 nPa) and low (<0.6 nPa) solar wind pressures with standard deviations, along with linear fits to the full dataset. Panel (b) shows a color plot of binned averages as a function of both solar photoionization frequency and solar wind pressure.

3.5. Variability of EIIF With Respect to In Situ Magnetic Field Conditions

So far we have examined broad patterns in nightside EIIF, both spatially and with respect to regional crustal magnetic field strength, that is, the magnitude of crustal field at 400 km above or below each measurement. While providing a broad picture, such an examination is not sensitive to fine-scale variability in EIIF due to the motions of ionizing electrons which are bound to magnetic field lines whose strength, direction and topology vary considerably over horizontal distances of tens of kilometers (<1° of latitude). Building geographic mean flux maps of sufficient horizontal and altitude resolution would take many dozens of years of observations. Instead, we can investigate the behavior of EIIF with respect to in situ measured magnetic field, particularly magnitude and elevation angle of the field, thus averaging together fluxes under all similar in situ magnetic field conditions. In this way, we can elucidate trends that should (on average) hold at any geographic location where such conditions are found.

Figure 11 plots EIIF with respect to magnetic field strength and elevation angle, for the same five altitude ranges and two solar wind pressure ranges as in Figure 9. Based on the analysis in the previous sections, we should expect crustal fields to reduce EIIF to a greater degree for stronger fields, and therefore to see a significant dependence of EIIF on magnetic field strength, at least for field strengths higher than that of the external magnetic fields (i.e., the draped IMF/magnetotail on the nightside). Also, we should expect steeper magnetic elevation angles, particularly for stronger fields, to correlate with higher EIIF since more vertical crustal magnetic fields can connect more easily with external fields and thus allow access to precipitating ionizing electrons, as shown by both Brain et al. (2007) and Lillis and Brain (2013). These expected properties are indeed generally what we see in Figure 11, however, with some features worth noting.

The most striking feature is the sharp decline (up to more than two orders of magnitude) in EIIF from upper left to lower right in all panels of Figure 11, that is, from weak to strong magnetic field and from high to low (i.e., steep to shallow) elevation angles. The most obvious explanation is that this reflects the transition between open magnetic field lines on which ionizing electrons can precipitate from the magnetosheath and tail, and closed field lines (loops) that they cannot access. The morphology of this transition is four dimensional, that is, it varies monotonically with respect to magnetic field strength, elevation angle, altitude, and solar wind pressure. Below (i.e., shallower than) a certain altitude-dependent critical elevation angle, EIIF drops sharply as magnetic field strength increases beyond a critical value. This critical magnetic field strength is approximately 15–20 nT for lower solar wind pressures and ~25 nT for higher solar wind pressures, or approximately twice the mean draped IMF fields shown in Figures 6a–6c, that is, the level where these more horizontal crustal fields start to dominate over draped fields, resulting in closed topology.

As altitude increases, the sharp transition occurs for lower elevation angles for magnetic field strengths above ~20 nT, that is, high EIIF can exist for progressively shallower magnetic elevation angles. This is a reflection of the fact that in regions of moderate or strong crustal magnetic field, open magnetic field regions increase in area as the magnetic field decays and diverges with increasing altitude above its source in the crust, much as a flower opens with distance above its stem. For example, below 160 km, there are almost no areas where field lines are open, even when they are vertical and strong. Between 160 and 200 km, only the steepest magnetic elevation angles (>~75°) are generally open for |B| > 20 nT. As altitude increases above 200 km, progressively shallower elevation angles are open until most of those above 30° are open between 400 and 500 km. We note that the trends in nightside magnetic field line topology that are likely responsible for the flux patterns we see were also demonstrated by Xu et al. (2017) using suprathermal electron spectra and by Weber et al. (2017) using suprathermal electron pitch angle distributions.

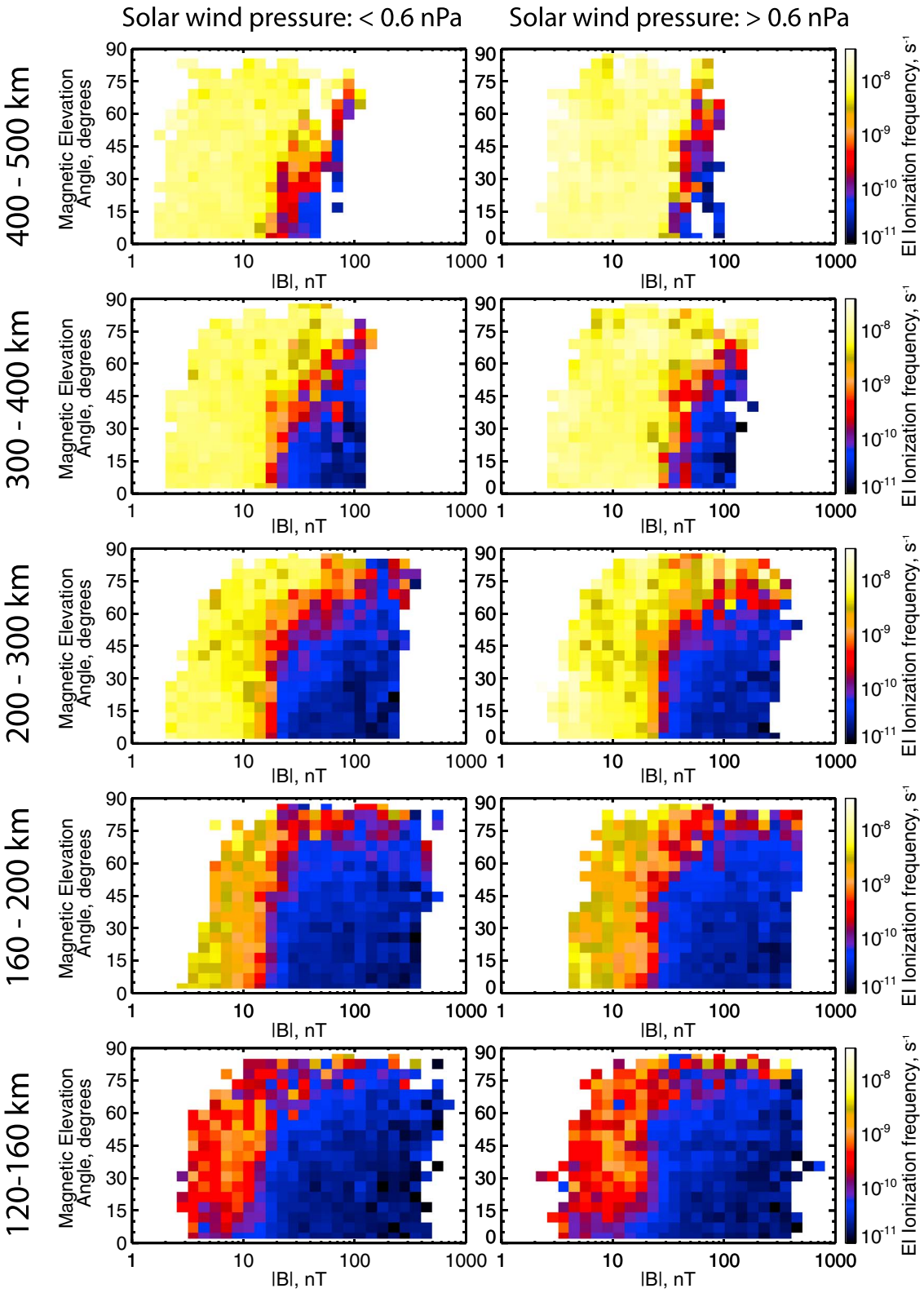


Figure 11. Mean electron impact ionization frequency is binned as a function of in situ measured magnetic field strength and elevation angle, separately by altitude range (rows: 120–160, 160–200, 200–300, 300–400, and 400–500 km) and solar wind pressure (columns: <0.6 and >0.6 nPa), for SZA > 115° and with the same color scale as shown in Figure 6. Note that 0° elevation angle corresponds to local horizontal and 90° elevation angle to local vertical. SZA = solar zenith angle.

Lastly, while it is expected that overall EIIF should be lower below 200 km due to absorption and backscattering of ionizing electrons by atmospheric neutrals, we note that for the most horizontal fields (elevation angle $<15°$) below 160 km, EIIF is very low for all magnetic field strengths, not just where closed crustal fields keep electrons out. It may be that there is simply no conduit for ionizing sheath or tail electrons from higher altitudes to reach such horizontal magnetic field lines so deep in the collisional atmosphere.

4. Discussion and Conclusions

In this paper we have investigated the behavior of CO_2 electron impact ionization frequency (EIIF) on the Martian nightside upper atmosphere. We characterized the spatial patterns of EIIF and its behavior with respect to altitude, SZA, solar wind pressure, and the strength and geometry of crustal magnetic fields. We have thus revealed a multidimensional but mostly intuitively understandable behavior governed primarily by (a) absorption and backscatter by atmospheric neutrals below ~200 km and (b) magnetic field topology which allows or retards the access of ionizing electrons to certain regions. This field topology is dynamic and varies with solar wind conditions, allowing greater ionizing electron access at higher altitudes and also for higher solar wind pressures, which compress closed crustal magnetic field loops, pushing them to lower altitudes.

Our motivation for this study is to better understand the magnitudes, patterns, and variability of electron impact ionization on the Martian nightside. Currently, this important source of energy is not accounted for in any global circulation model of the thermosphere and ionosphere (Bougher et al., 2015; Gonzalez-Galindo et al., 2013). In future work we would like to construct an empirical model of the average behavior of electron impact ionization frequency of CO_2 and O (the dominant gases below and above ~200 km, respectively) with respect to the variables investigated in this study, so that it may be used in such global circulation models to further improve our still-limited understanding of the nightside ionosphere and thermosphere of Mars.

Acknowledgments
We acknowledge the support of the MAVEN project for the work reflected in this manuscript. All data used in this manuscript are publicly available and can be found at the Planetary Data System website: https://pds.nasa.gov/tools/subscription_service/SS-20171115.shtml.

References

Bertaux, J. L., Leblanc, F., Witasse, O., Quemerais, E., Lilensten, J., Stern, S. A., et al. (2005). Discovery of an aurora on Mars. *Nature*, *435*(7043), 790–794. https://doi.org/10.1038/nature03603

Bougher, S. W., Pawlowski, D., Bell, J. M., Nelli, S., McDunn, T., Murphy, J. R., et al. (2015). Mars Global Ionosphere-Thermosphere Model: Solar cycle, seasonal, and diurnal variations of the Mars upper atmosphere. *Journal of Geophysical Research: Planets*, *120*, 311–342. https://doi.org/10.1002/2014JE004715

Brain, D. A., Halekas, J. S., Peticolas, L. M., Lin, R. P., Luhmann, J. G., Mitchell, D. L., et al. (2006). On the origin of aurorae on Mars. *Geophysical Research Letters*, *33*, L01201. https://doi.org/10.1029/2005GL024782

Brain, D. A., Lillis, R. J., Mitchell, D. L., Halekas, J. S., & Lin, R. P. (2007). Electron pitch angle distributions as indicators of magnetic field topology near Mars. *Journal of Geophysical Research*, *112*, A09201. https://doi.org/10.1029/2007JA012435

Brain, D. A., McFadden, J. P., Halekas, J. S., Connerney, J. E. P., Bougher, S. W., Curry, S., et al. (2015). The spatial distribution of planetary ion fluxes near Mars observed by MAVEN. *Geophysical Research Letters*, *42*, 9142–9148. https://doi.org/10.1002/2015GL065293

Collinson, G. A., Mitchell, D., Glocer, A., Grebowsky, J., Peterson, W. K., Connerney, J., et al. (2015). Electric Mars: The first direct measurement of an upper limit for the Martian "polar wind" electric potential. *Geophysical Research Letters*, *42*(21), 9128–9134. https://doi.org/10.1002/2015GL065084

Connerney, J. E. P., Espley, J., Lawton, P., Murphy, S., Odom, J., Oliversen, R., & Sheppard, D. (2015). The MAVEN magnetic field investigation. *Space Science Reviews*, *195*(1-4), 257–291. https://doi.org/10.1007/s11214-015-0169-4

Dong, Y., Fang, X., Brain, D. A., McFadden, J. P., Halekas, J. S., Connerney, J. E., et al. (2015). Strong plume fluxes at Mars observed by MAVEN: An important planetary ion escape channel. *Geophysical Research Letters*, *42*, 8942–8950. https://doi.org/10.1002/2015gl065346

Dubinin, E., Fraenz, M., Pätzold, M., McFadden, J., Halekas, J. S., DiBraccio, G. A., et al. (2017). The effect of solar wind variations on the escape of oxygen ions from Mars through different channels: MAVEN observations. *Journal of Geophysical Research: Space Physics*, *122*(11), 11,285–11,301. https://doi.org/10.1002/2017JA024741

Elrod, M. K., Bougher, S., Bell, J., Mahaffy, P. R., Benna, M., Stone, S., et al. (2017). He bulge revealed: He and CO_2 diurnal and seasonal variations in the upper atmosphere of Mars as detected by MAVEN NGIMS. *Journal of Geophysical Research: Space Physics*, *122*, 2564–2573. https://doi.org/10.1002/2016JA023482

Eparvier, F., Chamberlin, P. C., & Woods, T. N. (2015). The solar extreme ultraviolet monitor for MAVEN. *Space Science Reviews*, *195*(1–4), 293–301. https://doi.org/10.1007/s11214-015-0195-2

Fillingim, M. O., Lillis, R. J., England, S. L., Peticolas, L. M., Brain, D. A., Halekas, J. S., et al. (2012). On wind-driven electrojets at magnetic cusps in the nightside ionosphere of Mars. *Earth, Planets and Space*, *64*(2), 93–103. https://doi.org/10.5047/eps.2011.04.010

Fillingim, M. O., Peticolas, L. M., Lillis, R. J., Brain, D. A., Halekas, J. S., Lummerzheim, D., & Bougher, S. W. (2010). Localized ionization patches in the nighttime ionosphere of Mars and their electrodynamic consequences. *Icarus*, *206*(1), 112–119. https://doi.org/10.1016/j.icarus.2009.03.005

Fox, J. L., & Bakalian, F. (2001). Photochemical escape of atomic carbon from Mars. *Journal of Geophysical Research*, *106*(A12), 28,785–28,795. https://doi.org/10.1029/2001JA000108

Fox, J. L., & Hać, A. B. (2009). Photochemical escape of oxygen from Mars: A comparison of the exobase approximation to a Monte Carlo method. *Icarus*, *204*(2), 527–544. https://doi.org/10.1016/j.icarus.2009.07.005

Fu, H. S., Cao, J. B., Yang, B., & Lu, H. Y. (2011). Electron loss and acceleration during storm time: The contribution of wave-particle interaction, radial diffusion, and transport processes. *Journal of Geophysical Research*, *116*, A10210. https://doi.org/10.1029/2011JA016672

Girazian, Z., Mahaffy, P., Lillis, R. J., Benna, M., Elrod, M., Fowler, C. M., & Mitchell, D. L. (2017). Ion densities in the nightside ionosphere of Mars: Effects of electron impact ionization. *Geophysical Research Letters*, *44*(22), 11,248–11,256. https://doi.org/10.1002/2017GL075431

Girazian, Z., Mahaffy, P. R., Lillis, R. J., Benna, M., Elrod, M., & Jakosky, B. M. (2017). Nightside ionosphere of Mars: Composition, vertical structure, and variability. *Journal of Geophysical Research: Space Physics*, *122*, 4712–4725. https://doi.org/10.1002/2016JA023508

Gonzalez-Galindo, F., Chaufray, J. Y., Lopez-Valverde, M. A., Gilli, G., Forget, F., Leblanc, F., et al. (2013). Three-dimensional Martian ionosphere model: I. The photochemical ionosphere below 180 km. *Journal of Geophysical Research: Planets*, *118*(10), 2105–2123, https://doi.org/10.1002/Jgre.20150

Halekas, J. S., Ruhunusiri, S., Harada, Y., Collinson, G., Mitchell, D. L., Mazelle, C., et al. (2017). Structure, dynamics, and seasonal variability of the Mars-solar wind interaction: MAVEN Solar Wind Ion Analyzer in-flight performance and science results. *Journal of Geophysical Research: Space Physics*, *122*, 547–578. https://doi.org/10.1002/2016JA023167

Halekas, J. S., Taylor, E. R., Dalton, G., Johnson, G., Curtis, D. W., McFadden, J. P., et al. (2015). The Solar Wind Ion Analyzer for MAVEN. *Space Science Reviews*, *195*(1-4), 125–151. https://doi.org/10.1007/s11214-013-0029-z

Jakosky, B. M., Lin, R. P., Grebowsky, J. M., Luhmann, J. G., Mitchell, D. F., Beutelschies, G., et al. (2015). The Mars Atmosphere and Volatile Evolution (MAVEN) mission. *Space Science Reviews*, *195*(1-4), 3–48. https://doi.org/10.1007/s11214-015-0139-x

Leblanc, F., Modolo, R., Curry, S., Luhmann, J., Lillis, R., Chaufray, J. Y., et al. (2015). Mars heavy ion precipitating flux as measured by Mars Atmosphere and Volatile EvolutioN. *Geophysical Research Letters*, *42*, 9135–9141. https://doi.org/10.1002/2015GL066170

Leblanc, F., Witasse, O., Winningham, J., Brain, D., Lilensten, J., Blelly, P. L., et al. (2006). Origins of the Martian aurora observed by Spectroscopy for Investigation of Characteristics of the Atmosphere of Mars (SPICAM) on board Mars Express. *Journal of Geophysical Research*, *111*, A09313. https://doi.org/10.1029/2006JA011763

Lee, Y., Combi, M. R., Tenishev, V., & Bougher, S. W. (2014). Hot carbon corona in Mars' upper thermosphere and exosphere: 1. Mechanisms and structure of the hot corona for low solar activity at equinox. *Journal of Geophysical Research: Planets*, *119*(5), 905–924. https://doi.org/10.1002/2013JE004552

Lee, Y., Combi, M. R., Tenishev, V., Bougher, S. W., & Lillis, R. J. (2015). Hot oxygen corona at Mars and the photochemical escape of oxygen: Improved description of the thermosphere, ionosphere, and exosphere. *Journal of Geophysical Research: Planets*, *120*, 1880–1892. https://doi.org/10.1002/2015JE004890

Lillis, R. J., & Brain, D. A. (2013). Nightside electron precipitation at Mars: Geographic variability and dependence on solar wind conditions. *Journal of Geophysical Research: Space Physics*, *118*, 3546–3556. https://doi.org/10.1002/jgra.50171

Lillis, R. J., Brain, D. A., Bougher, S. W., Leblanc, F., Luhmann, J. G., Jakosky, B. M., et al. (2015). Characterizing atmospheric Escape from Mars today and through time, with MAVEN. *Space Science Reviews*, *195*(1-4), 357–422. https://doi.org/10.1007/s11214-015-0165-8

Lillis, R. J., Deighan, J., & Fox, J. (2017). Photochemical escape of oxygen from Mars: First results from MAVEN in situ data. *Journal of Geophysical Research: Space Physics*, *122*, 3815–3836. https://doi.org/10.1002/2016JA023525

Lillis, R. J., Deighan, J., Fox, J. L., Bougher, S. W., Lee, Y., Combi, M. R., et al. (2017). Photochemical escape of oxygen from Mars: First results from MAVEN in situ data. *Journal of Geophysical Research: Space Physics*, *122*, 3815–3836. https://doi.org/10.1002/2016JA023525

Lillis, R. J., & Fang, X. (2015). Electron impact ionization in the Martian atmosphere: Interplay between scattering and crustal magnetic field effects. *Journal of Geophysical Research: Planets*, *120*, 1332–1345. https://doi.org/10.1002/2015JE004841

Lillis, R. J., Fillingim, M. O., & Brain, D. A. (2011). Three-dimensional structure of the Martian nightside ionosphere: Predicted rates of impact ionization from Mars Global Surveyor magnetometer and electron reflectometer measurements of precipitating electrons. *Journal of Geophysical Research*, *116*, A12317. https://doi.org/10.1029/2011JA016982

Lillis, R. J., Fillingim, M. O., Peticolas, L. M., Brain, D. A., Lin, R. P., & Bougher, S. W. (2009). Nightside ionosphere of Mars: Modeling the effects of crustal magnetic fields and electron pitch angle distributions on electron impact ionization. *Journal of Geophysical Research*, *114*, E11009. https://doi.org/10.1029/2009JE003379

Lillis, R. J., Halekas, J. S., Fillingim, M. O., Poppe, A. R., Collinson, G., Brain David, A., & Mitchell, D. L. (2018). Field-aligned electrostatic potentials above the Martian exobase from MGS electron reflectometry: Structure and variability. *Journal of Geophysical Research: Planets*, *123*(1), 67–92. https://doi.org/10.1002/2017JE005395

Lillis, R. J., Mitchell, D. L., Lin, R. P., & Acuna, M. H. (2008). Electron reflectometry in the martian atmosphere. *Icarus*, *194*(2), 544–561. https://doi.org/10.1016/j.icarus.2007.09.030

Lillis, R. J., Mitchell, D. L., Lin, R. P., Connerney, J. E. P., & Acuna, M. H. (2004). Mapping crustal magnetic fields at Mars using electron reflectometry. *Geophysical Research Letters*, *31*, L15702. https://doi.org/10.1029/2004GL020189

Luhmann, J. G., Johnson, R. E., & Zhang, M. H. G. (1992). Evolutionary impact of sputtering of the Martian atmosphere by O^+ pickup ions. *Geophysical Research Letters*, *19*, 2151–2154. https://doi.org/10.1029/92GL02485

Lundin, R., Barabash, S., Dubinin, E., Winningham, D., & Yamauchi, M. (2011). Low-altitude acceleration of ionospheric ions at Mars. *Geophysical Research Letters*, *38*, L08108. https://doi.org/10.1029/2011GL047064

Lundin, R., Barabash, S., Holmstrom, M., Nilsson, H., Futaana, Y., Ramstad, R., et al. (2013). Solar cycle effects on the ion escape from Mars. *Geophysical Research Letters*, *40*, 6028–6032. https://doi.org/10.1002/2013GL058154

Lundin, R., Barabash, S., Holmstrom, M., Nilsson, H., Yamauchi, M., Fraenz, M., & Dubinin, E. M. (2008). A comet-like escape of ionospheric plasma from Mars. *Geophysical Research Letters*, *35*, L18203. https://doi.org/10.1029/2008GL034811

Lundin, R., Zakharov, A., Pellinen, R., Borg, H., Hultqvist, B., Pissarenko, N., et al. (1989). First measurements of the ionospheric plasma escape from Mars. *Nature*, *341*(6243), 609–612. https://doi.org/10.1038/341609a0

Mahaffy, P. R., Benna, M., King, T., Harpold, D. N., Arvey, R., Barciniak, M., et al. (2014). The neutral gas and ion mass spectrometer on the Mars Atmosphere and Volatile Evolution mission. *Space Science Reviews*, *195*(1-4), 49–73. https://doi.org/10.1007/s11214-014-0091-1

Mitchell, D. L., Lin, R. P., Mazelle, C., Rème, H., Cloutier, P. A., Connerney, J. E. P., et al. (2001). Probing Mars' crustal magnetic field and ionosphere with the MGS Electron Reflectometer. *Journal of Geophysical Research*, *106*, 23,419–23,427. https://doi.org/10.1029/2000JE001435

Mitchell, D. L., Mazelle, C., Sauvaud, J. A., Thocaven, J. J., Rouzaud, J., Fedorov, A., et al. (2016). The MAVEN Solar Wind Electron Analyzer. *Space Science Reviews*, *200*(1-4), 495–528. https://doi.org/10.1007/s11214-015-0232-1

Morschhauser, A., Lesur, V., & Grott, M. (2014). A spherical harmonic model of the lithospheric magnetic field of Mars. *Journal of Geophysical Research: Planets*, *119*, 1162–1188. https://doi.org/10.1002/2013JE004555

Nagy, A. F., Winterhalter, D., Sauer, K., Cravens, T. E., Brecht, S., Mazelle, C., et al. (2004). The plasma environment of Mars. *Space Science Reviews*, *111*(1/2), 33–114. https://doi.org/10.1023/B:Spac.0000032718.47512.92

Němec, F., Morgan, D. D., Gurnett, D. A., & Brain, D. A. (2011). Areas of enhanced ionization in the deep nightside ionosphere of Mars. *Journal of Geophysical Research*, *116*, E06006. https://doi.org/10.1029/2011JE003804

Němec, F., Morgan, D. D., Gurnett, D. A., & Duru, F. (2010). Nightside ionosphere of Mars: Radar soundings by the Mars Express spacecraft. *Journal of Geophysical Research*, *115*, E12009. https://doi.org/10.1029/2010JE003663

Riedler, W., Möhlmann, D., Oraevsky, V. N., Schwingenschuh, K., Yeroshenko, Y., Rustenbach, J., et al. (1989). Magnetic-fields near Mars: First results. *Nature*, *341*(6243), 604–607. https://doi.org/10.1038/341604a0

Riousset, J. A., Paty, C. S., Lillis, R. J., Fillingim, M. O., England, S. L., Withers, P. G., & Hale, J. P. M. (2014). Electrodynamics of the Martian dynamo region near magnetic cusps and loops. *Geophysical Research Letters*, *41*, 1119–1125. https://doi.org/10.1002/2013GL059130

Safaeinili, A., Kofman, W., Mouginot, J., Gim, Y., Herique, A., Ivanov, A. B., et al. (2007). Estimation of the total electron content of the Martian ionosphere using radar sounder surface echoes. *Geophysical Research Letters*, *34*, L23204. https://doi.org/10.1029/2007GL032154

Schneider, N. M., Deighan, J. I., Jain, S. K., Stiepen, A., Stewart, A. I. F., Larson, D., et al. (2015). Discovery of diffuse aurora on Mars. *Science*, *350*(6261), aad0313. https://doi.org/10.1126/science.aad0313

Shane, A. D., Xu, S. S., Liemohn, M., & Mitchell, D. L. (2016). Mars nightside electrons over strong crustal fields. *Journal of Geophysical Research: Space Physics*, *121*(4), 3808–3823. https://doi.org/10.1002/2015JA021947

Steckiewicz, M., Garnier, P., André, N., Mitchell, D. L., Andersson, L., Penou, E., et al. (2017). Comparative study of the Martian suprathermal electron depletions based on Mars Global Surveyor, Mars Express, and Mars Atmosphere and Volatile EvolutioN mission observations. *Journal of Geophysical Research: Space Physics*, *122*, 857–873. https://doi.org/10.1002/2016JA023205

Steckiewicz, M., Mazelle, C., Garnier, P., André, N., Penou, E., Beth, A., et al. (2015). Altitude dependence of nightside Martian suprathermal electron depletions as revealed by MAVEN observations. *Geophysical Research Letters*, *42*, 8877–8884. https://doi.org/10.1002/2015GL065257

Sung, K., & Fox, J. L. (2000). Electron impact cross sections for use in modeling the ionospheres/thermospheres of the earth and planets, Eos Trans. AGU, 8418 Fall Meeting supplement, SA52A-11.

Thiemann, E. M. B., Chamberlin, P. C., Eparvier, F. G., Templeman, B., Woods, T. N., Bougher, S. W., & Jakosky, B. M. (2017). The MAVEN EUVM model of solar spectral irradiance variability at Mars: Algorithms and results. *Journal of Geophysical Research: Space Physics*, *122*, 2748–2767. https://doi.org/10.1002/2016ja023512

Weber, T., Brain, D., Mitchell, D. L., Xu, S., Connerney, J., & Halekas, J. (2017). Characterization of low-altitude nightside Martian magnetic topology using electron pitch angle distributions. *Journal of Geophysical Research: Space Physics*, *122*(10), 9777–9789. https://doi.org/10.1002/2017JA024491

Xu, S. S., Mitchell, D., Liemohn, M., Dong, C., Bougher, S., Fillingim, M., et al. (2016). Deep nightside photoelectron observations by MAVEN SWEA: Implications for Martian northern hemispheric magnetic topology and nightside ionosphere source. *Geophysical Research Letters*, *43*(17), 8876–8884. https://doi.org/10.1002/2016GL070527

Xu, S. S., Mitchell, D., Liemohn, M., Fang, X., Ma, Y., Luhmann, J., et al. (2017). Martian low-altitude magnetic topology deduced from MAVEN/SWEA observations. *Journal of Geophysical Research: Space Physics*, *122*, 1831–1852. https://doi.org/10.1002/2016JA023467